
First Results from Cryogenic Target Implosions on OMEGA

Introduction

The base-line direct-drive ignition target design for the National Ignition Facility (NIF)¹ is a thick cryogenic DT-ice layer enclosed in a thin CH shell.^{2,3} In direct-drive inertial confinement fusion (ICF)⁴ a spherical target is illuminated by a large number of laser beams to provide a spherically symmetric implosion. Target implosions with cryogenic DT fuel are planned using the 60-beam OMEGA laser system⁵ to validate the theoretically determined³ levels of laser and target uniformity required to achieve direct-drive ignition and gain on the NIF. The OMEGA cryogenic target designs are energy scaled from the NIF ignition designs.^{2,3} In particular, the OMEGA cryogenic targets, driven by an energy-scaled ignition pulse, are designed to be as “hydrodynamically equivalent” as possible to the ignition capsule designs. In this context, the constraints placed on the OMEGA cryogenic target designs include peak shell velocities, hot-spot convergence, in-flight aspect ratio, and stability properties similar to those of the NIF designs. To compare igniting and non-igniting target designs, we use the hot-spot convergence ratio, defined as the ratio of the radius containing 90% of the yield when propagating burn was deactivated compared to the initial ice–gas interface. In addition, the principle sources of nonuniformity on OMEGA, which lead to a degradation in target performance, are similar to the NIF. For direct-drive ICF these sources are single-beam nonuniformity (“laser imprint”), drive asymmetry, inner ice surface, and outer-surface roughness.

Ignition with direct-drive ICF relies on the generation of a “spark” in the compressed “hot spot” to begin the nuclear burn.⁶ The hot spot is a high-temperature, low-density region surrounded by a low-temperature, high-density region into which the burn wave propagates, leading to significant energy gain. Target and laser illumination nonuniformities lead to distortions in the hot spot due to secular (linear in time) growth of low-order ($\ell \leq 10$) modes, shell breakup, and mix due to the Rayleigh–Taylor (RT)^{7,8} growth of high-order ($\ell > 10$) nonuniformities. Previous cryogenic target experiments^{9–13} have used ice layers that were formed only by β -layering, but not thoroughly and carefully characterized. The targets gener-

ally performed poorly (the reported neutron yields did not exceed 0.2% of the 1-D predictions¹⁰), and the results could not be used to validate detailed multidimensional numerical simulations because of the missing information on the inner-ice-surface nonuniformity spectrum.

This article describes first experiments with layered and characterized cryogenic targets on OMEGA. These experiments have validated the technology to fill, layer, characterize, and shoot cryogenic targets. The following sections present the OMEGA cryogenic target designs, describe the results of the characterization of the inner-ice-surface quality of the cryogenic targets, review the results from the first cryogenic D₂ campaign on OMEGA, give an outlook on future improvements, and present conclusions.

OMEGA Cryogenic Target Designs

The basis for the OMEGA cryogenic designs is the NIF direct-drive, $\alpha = 3$ ignition design, which consists of a 340- μm -thick DT-ice layer encased in a thin (3- μm) plastic capsule of 1.69-mm outer radius.³ The laser pulse required for the ignition design is a 9.25-ns shaped pulse consisting of a 10-TW, 4.25-ns foot rising to a 450-TW peak drive for 2.5 ns. Although higher one-dimensional gains can be achieved for lower-adiabat implosions, the highest multidimensional gains for NIF energy and uniformity levels are predicted to be achieved for implosions driven on an adiabat between 3 and 4. One-dimensional hydrodynamic scaling arguments¹⁴ have been used to design the cryogenic targets for OMEGA. It has been shown^{14,15} that the energy, time, and laser power scalings are

$$(E \sim R^3, t \sim R, \text{ and } P \sim R^2).$$

The NIF is designed to provide 1.5 MJ of energy with the $\alpha = 3$ pulse shape, while OMEGA is capable of delivering 30 kJ. Thus, the radius of an OMEGA capsule should be approximately 0.3 times the NIF design, i.e., 0.46 mm, with a 100- μm DT-ice layer inside a 1- μm -thick plastic shell. The equivalent OMEGA $\alpha = 3$ pulse consists of a 0.75-TW foot

rising to a 33-TW peak with an overall pulse length of 2.5 ns. Figure 90.1 shows a comparison between the NIF and OMEGA targets and pulse shapes. One-dimensional hydrocode calculations predict a gain of 45 (neutron yield $Y_n = 2.5 \times 10^{19}$), a hot-spot convergence ratio of 28, and a peak fuel areal density $\rho R_{\text{peak}} = 1300 \text{ mg/cm}^2$ for the NIF ignition design. A neutron yield of $Y_n = 1.8 \times 10^{14}$, a hot-spot convergence ratio of 20, and a peak fuel areal density $\rho R_{\text{peak}} = 300 \text{ mg/cm}^2$ are predicted for the scaled OMEGA cryogenic DT design.³ The “classical” definition of convergence ratio (the ratio of the minimum to the initial fuel–shell radius) is inappropriate for cryogenic targets since the inner ice layer forms part of the hot spot; therefore we use the hot-spot convergence ratio as defined in the introduction. A detailed analysis¹⁵ shows that the energy-scaled targets exhibit similar 1-D behavior of the shock timing and fuel adiabat as the ignition designs. The shorter density scale length of the OMEGA target leads to a lower laser energy absorption of 40% compared to 60% for the ignition design. Consequently the energy-scaled target has a slightly higher adiabat and a lower hot-spot convergence ratio of 20 compared to 28 in the ignition design.

The RT instability can degrade target performance by breaking the spherical symmetry of the implosion. The RT instability occurs twice during the implosion: at the outer ablation surface as the shell accelerates inward and at the hot spot/main fuel layer interface as the capsule decelerates at the end of the implosion. The RT instability is seeded by single-beam laser

nonuniformity, drive asymmetry, feedout from the inner ice surface, and outer-surface roughness. Detailed 2-D *ORCHID* simulations³ have established the maximum levels of these nonuniformity sources to achieve ignition and gain on the NIF.

The analysis of these results shows that, for an outer-surface roughness of <115 nm and an inner-ice-surface roughness of $\leq 1 \mu\text{m}$ rms, individual beam smoothing by two-color-cycle, 1-THz, 2-D SSD with polarization smoothing (PS), and an on-target power imbalance of <2% rms, a gain of 30 is predicted for the NIF (70% of 1-D). The OMEGA design has been shown^{3,15} to be more sensitive to the nonuniformity seeds than the NIF. This is attributed to the smaller hot spot in the OMEGA design, which can be more easily disrupted by the penetration of the cold spikes from the main fuel layer. For the same uniformity conditions as described for the NIF, the OMEGA-scaled $\alpha = 3$ design is predicted to give 30% of 1-D yield.¹⁵

Target Layering and Characterization

To create a 100- μm ice layer, the $\sim 3\text{-}\mu\text{m}$ -thick, high-strength CH shells were filled with ~ 1000 atm of D_2 in a permeation cell inside the Fill/Transfer Station (FTS).¹⁶ The process of filling these capsules takes ~ 24 h because the gas pressure can be incremented only in very small steps (0.7 atm/min) to avoid buckling of the thin shell due to the pressure gradient between higher pressure outside and lower pressure inside the targets. The targets are cooled very slowly (~ 0.1 K/min) to below the triple point of D_2 (18.72 K) to avoid bursting from the higher

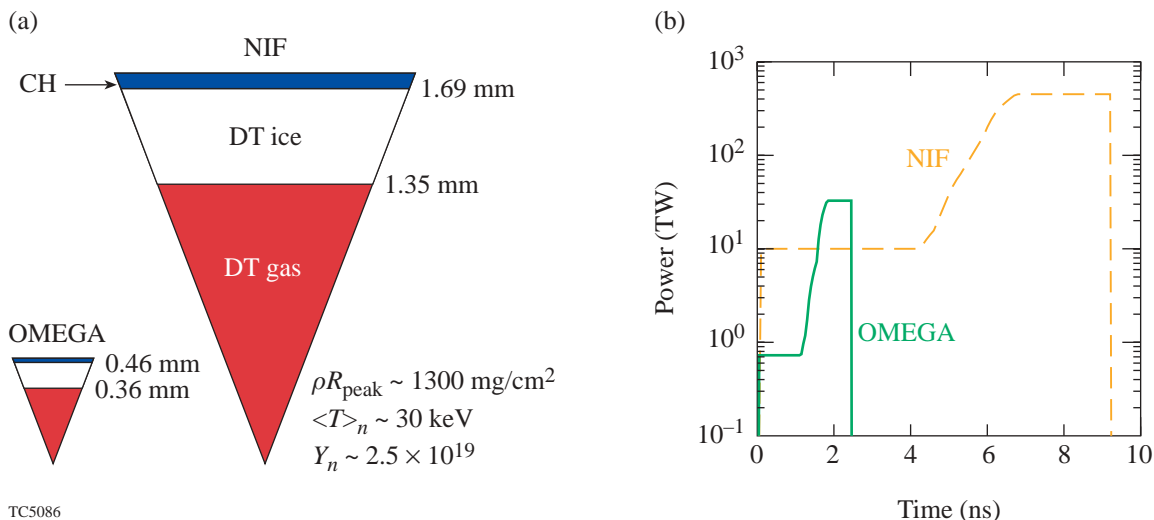


Figure 90.1 The NIF and OMEGA capsule designs (a) and pulse shapes (b). The radius of the OMEGA design is approximately 0.3 times that for the NIF. The pulse duration shrinks from 9.25 ns with a peak power of 450 TW to 2.5 ns with 32-TW peak power.

pressure of the warmer gas inside the targets. After transferring the targets from the FTS to the moving cryostat transfer cart (MCTC), the target assembly is inserted into the characterization station, where the targets are viewed using a high-magnification, high-fidelity optical system during the layering process. The layer is formed and maintained using an IR laser at $3.16\text{-}\mu\text{m}$ wavelength, which is preferentially absorbed in the D_2 ice. This creates a temperature gradient between the cooled layering sphere, which surrounds the target, and the gas/ice interface inside the target. Thicker parts of the ice layer are heated preferentially, increasing the sublimation rate in the hotter parts, while the gas preferentially refreezes at the colder parts of the ice layer. This results in a net layering effect that leads to an equal ice-layer thickness over the entire sphere.

This IR layering scheme uses more than one order of magnitude more heating power than β -layering of DT-filled cryogenic targets can provide, which suggests that active layering might be necessary even for DT targets.

The inner-ice-surface nonuniformities are characterized using a shadowgraphic technique as shown in Fig 90.2. The parallel rays from a light source are refracted at the plastic shell and reflected by total internal reflection from the inner ice surface, thus forming a virtual bright ring. The bright ring in the recorded image is unrolled using the center of the shadow of the plastic shell as a reference point, providing a graph with the distance of the inner ice surface from the center of the shell as a function of angle. The difference in the measured distance of

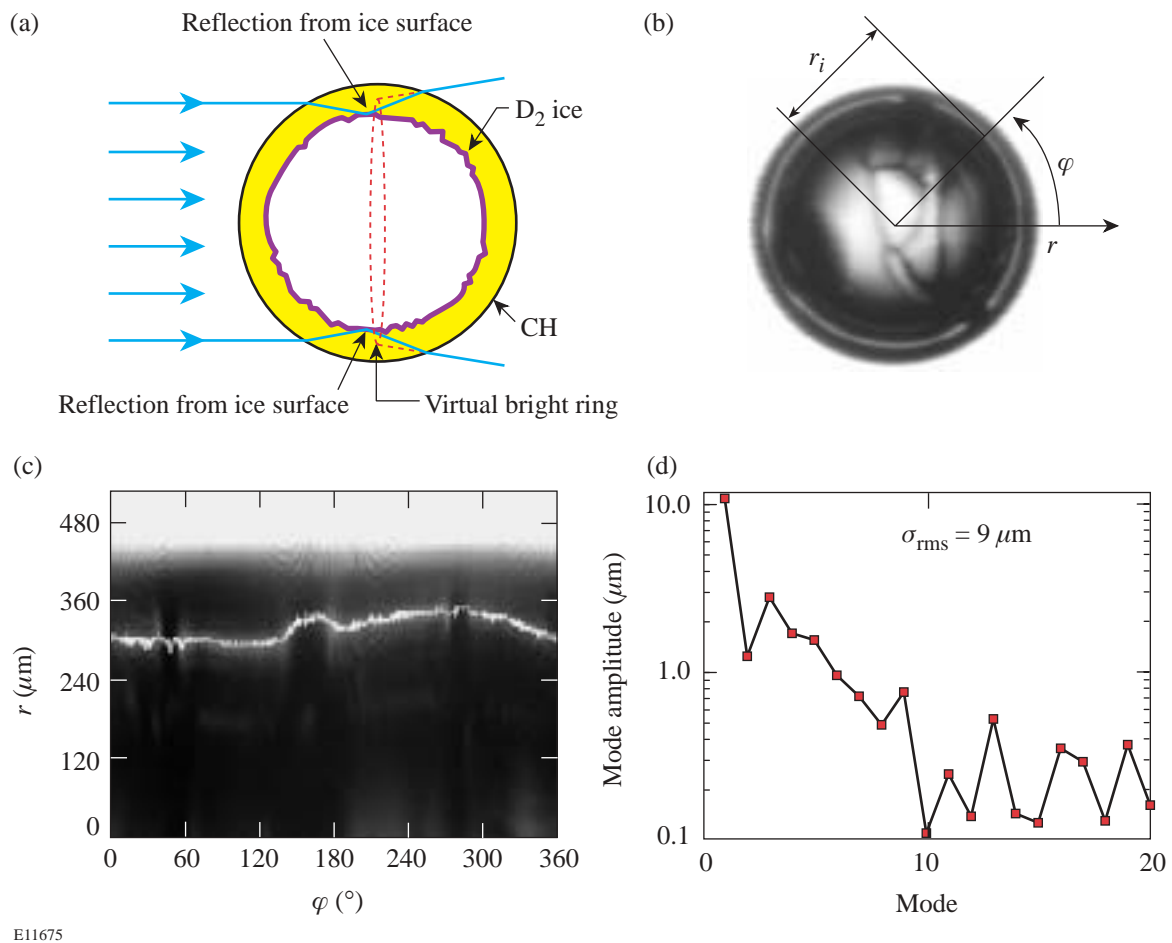


Figure 90.2

Shadowgraphic layer characterization: (a) The target is illuminated by collimated white light. (b) Internal total reflection at the ice/gas surface produces a virtual bright ring in the image. (c) The image is unrolled around its center, mapping the distance of the ice/gas interface as a function of angle around the target. (d) The difference of the measured distance from a perfect circle is decomposed into cosine mode amplitudes.

the ice surface from a perfect circle is then decomposed into cosine modes, resulting in a nonuniformity spectrum of the inner ice surface. These measurements provide only a 2-D representation of the inner-ice-surface nonuniformity along one circular cut through the sphere. Several such measurements, along different lines of sight, can be performed to fully map the 3-D nonuniformity spectrum.

Cryogenic Target Implosions

The cryogenic targets used in these first experiments were $\sim 930\text{-}\mu\text{m}$ -diam, $\sim 3\text{-}\mu\text{m}$ -thick shells of high-strength CH with $100\text{-}\mu\text{m}$ -thick D_2 -ice layers. The targets were characterized along one line of sight and showed an inner-ice-surface roughness of $\sigma_{\text{rms}} \geq 9\ \mu\text{m}$, with the most power ($\sim 90\%$) in the three lowest modes. A 1-ns square pulse at $\sim 24\text{-kJ}$ laser energy was used with the best single-beam smoothing available [distributed phase plates (DPP);¹⁷ polarization smoothing (PS) with birefringent wedges;¹⁸ 2-D, single-color-cycle, 1-THz smoothing by spectral dispersion (SSD)¹⁹] and optimized energy balance ($<3\%$ beam to beam).²⁰ The calculated time-dependent, on-target overlapped nonuniformity ($\ell = 1 \sim 500$) due to single-beam nonuniformity, assuming perfect beam-to-beam power balance for 1-THz SSD with PS, is less than 1% after 300 ps.²¹ When beam overlap on target is included, the on-target nonuniformity due to beam-to-beam energy imbalance is less than 1% ($\ell \leq 12$). This level of single-beam laser nonuniformity and drive asymmetry is close to that specified above; however, the current levels of inner-ice-surface roughness ($\sigma_{\text{rms}} \geq 9\ \mu\text{m}$) significantly exceed the design goal ($\sigma_{\text{rms}} \leq 1\ \mu\text{m}$). A 1-ns square pulse was used to make the implosion

less sensitive to instability growth than the $\alpha = 3$ design in Fig. 90.1. This pulse puts the target on an $\alpha = 25$ adiabat and leads to a predicted hot-spot convergence ratio of approximately 10. One-dimensional *LILAC*²² simulations predict a neutron-averaged areal density of $\sim 40\ \text{mg}/\text{cm}^2$, an ion temperature of approximately 2 keV, and a neutron yield of 1.0×10^{11} . Five target shots were successfully performed in a two-week experimental campaign. All targets showed good neutron-yield performance (up to 3.5×10^{10}), ranging from 4% to 30% of the clean yield, denoted as yield over clean (YOC), predicted by 1-D *LILAC* hydrodynamic simulations.

Table 90.I summarizes the performance measured by neutron and particle diagnostics of two target shots, 24089 and 24096, having ice-layer nonuniformities of $\sigma_{\text{rms}} = 19\ \mu\text{m}$ and $\sigma_{\text{rms}} = 9\ \mu\text{m}$, respectively. The performance is compared with 1-D clean calculations. Secondary in-flight fusion reactions of the tritium (T) and helium (He^3) ions produced in the D_2 fusion reaction can be used to infer fuel areal densities.^{23–26} The areal density of the hot neutron-producing core $\langle \rho R \rangle_{\text{hot}}$ ($T_i \geq 0.5\ \text{keV}$) is inferred using the ratio of the secondary proton to the primary neutron, Y_{2p}/Y_n , from the in-flight fusion of He^3 (Ref. 27). Due to the very short range of He^3 in the colder fuel ($< 1\ \text{mg}/\text{cm}^2$ at $T_e < 0.5\ \text{keV}$),²⁸ the secondary proton production is confined to the hot parts of the core, if the electron and ion temperatures are assumed to be equal. This measurement saturates at about $10\ \text{mg}/\text{cm}^2$ for a plasma electron temperature close to 3 keV, which is consistent with the measured neutron-averaged ion temperatures $\langle T_{\text{ion}} \rangle_n$. The inferred values of $\langle \rho R \rangle_{\text{hot}} = 5\ \text{mg}/\text{cm}^2$ and $\langle \rho R \rangle_{\text{hot}} = 7\ \text{mg}/\text{cm}^2$ for target shots

Table 90.I: Target performance measured by neutron and particle diagnostics and compared to 1-D clean calculations for the two best-performing target shots: 24089 and 24096.

	1-D	24089	24096
Roughness (μm)		19	9
Neutron yield	1.0×10^{11}	$(1.26 \pm 0.1) \times 10^{10}$	$(3.05 \pm 0.1) \times 10^{10}$
Yield compared to 1-D		16%	30%
$\langle T_{\text{ion}} \rangle_n$ (keV)	2.1	2.9 ± 0.5	3.5 ± 0.5
Bang time (ns)	1.8	1.8 ± 0.1	1.7 ± 0.1
Y_{2n}/Y_n	9.0×10^{-3}	$(8.0 \pm 0.4) \times 10^{-3}$	$(9.0 \pm 0.5) \times 10^{-3}$
Y_{2p}/Y_n	1.2×10^{-3}	$(0.6 \pm 0.1) \times 10^{-3}$	$(0.8 \pm 0.1) \times 10^{-3}$
$\langle \rho R \rangle_{\text{hot}}$ (mg/cm^2)	14	5 ± 1	7 ± 1
$\langle \rho R \rangle_{\text{total}}$ (mg/cm^2)	40	20–30–58	12–25–38

24089 and 24096, respectively, are well below the saturation level. The predicted areal density of the hot neutron-producing core $\langle \rho R \rangle_{\text{hot}}$ ($T_i \geq 0.5$ keV) at peak neutron production in the 1-D clean calculations is 14 mg/cm^2 . The total areal density $\langle \rho R \rangle_{\text{total}}$ is measured using the downshift of the secondary proton spectrum.²⁷ A relatively large spread is seen in the data, recorded by five proton detectors located in different ports around the target. Table 90.I shows the minimum, average, and maximum values inferred. The predicted 1-D $\langle \rho R \rangle_{\text{total}}$ is given by the neutron-averaged areal density. The measured average total areal densities are more than 60% of the 1-D clean predictions. The ratio of the secondary neutron to the primary neutron, Y_{2n}/Y_n , can also be used to infer the total areal density.^{25,27} However, secondary neutron ratios are also sensitive to the temperature profile through the slowing down of the primary triton of the D_2 fusion reaction and the energy-dependent cross section of the reaction. In these experiments it is most probably saturated, given the relatively high $\langle \rho R \rangle_{\text{total}}$ as inferred from the downshift of the secondary proton spectrum. In addition, secondary neutron ratios close to 1×10^{-2} are seen in this model only if all the fuel has a temperature higher than 1 keV,^{25,28} which is a highly unlikely scenario in these experiments. The measured and predicted bang times are very

close, indicating that the laser absorption and hydrodynamic response of the cryogenic targets are accurately modeled in the 1-D clean calculations. The experimental data show that the YOC and $\langle \rho R \rangle_{\text{hot}}$ are most sensitive to the inner-ice-surface nonuniformities and improve significantly as the nonuniformity decreases. The neutron-averaged ion temperature and the bang time exhibit little sensitivity to the ice nonuniformity. Figure 90.3 shows static x-ray pinhole camera (XRPC) images and snapshots taken by an x-ray framing camera (XRFC) with an exposure time of 40 ps at peak compression compared with shadowgraphic images taken before the target shot. The XRPC images display the entire implosion from the thin plastic shell lighting up on the outside of the target at the beginning of the pulse to the formation of a core in the center of the image. A comparison of the two experiments clearly shows that shot 24096 starts with lower inner-ice-surface nonuniformities that carry over into a more integral and symmetric core. Neutron data confirm this behavior with shot 24096 achieving 30% YOC while shot 24089 had 16% YOC. This should be compared to noncryogenic implosion experiments on OMEGA that have achieved YOC of $\sim 30\%$ for targets with acceleration-phase-stability properties similar to the future $\alpha = 3$ cryogenic implosions described earlier.²⁰

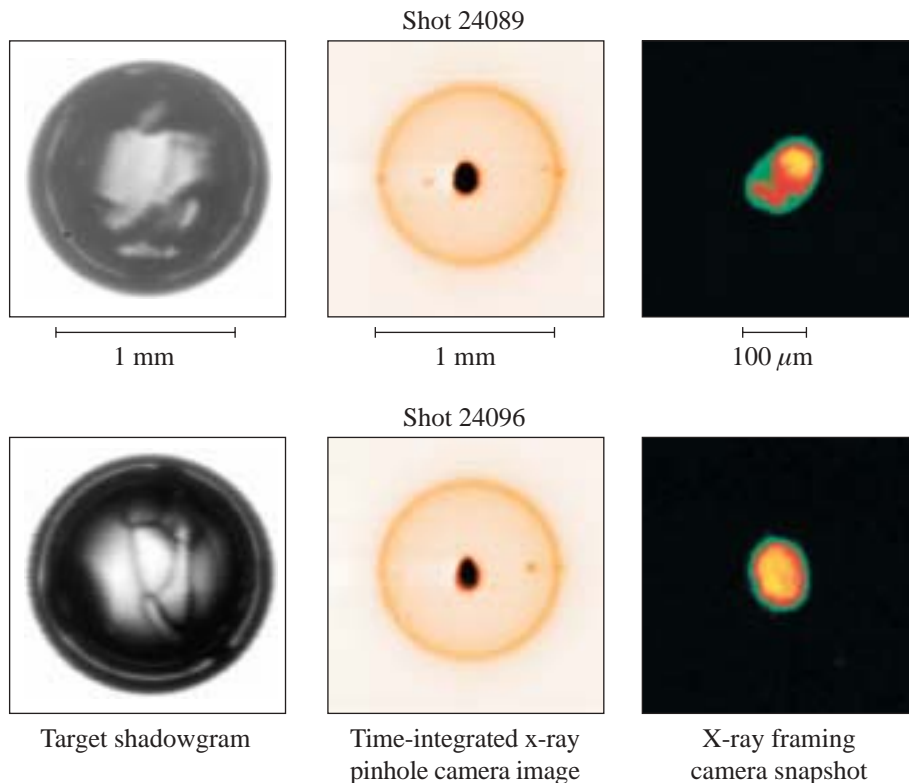


Figure 90.3

Shadowgraphic images of the targets for shots 24089 and 24096 shown in comparison with static x-ray pinhole camera (XRPC) images and x-ray framing camera (XRFC) snapshots. The XRPC images show the lighting up of the thin plastic shell on the outside of the target and the formation of a core in the center of the image. The XRFC images are recorded at peak compression with an exposure time of 40 ps. A clear correlation of the layer quality in the shadowgraphic images and the core quality in the XRPC and XRFC images can be seen.

E11249

Both the nuclear and x-ray data indicate that at the present level of inner-ice-surface nonuniformity, the target performance as measured by the YOC, the areal density of the hot neutron-producing core, and the integrity and symmetry of the x-ray core image are strongly affected by the quality of the inner ice layer. The other nonuniformity sources including laser imprint and drive asymmetry, which did not vary significantly during the experimental campaign, appear to be less important in these experiments.

Near-Term Developments

Recent layering studies have produced a much better layer quality ($\sigma_{rms} = 3 \mu\text{m}$), with most of the amplitude in the two lowest-order modes. Figure 90.4 shows a shadowgraphic image of such a layer, together with the mode-amplitude spectrum. If the two lowest-order modes of the inner-ice-surface nonuniformity are caused by nonuniformities in the tempera-

ture profile inside the layering sphere, they are relatively easy to improve by minor changes in the layout of the layering geometry.²⁹ Other sources of ice-surface nonuniformity, like enhanced thermal resistivity at the plastic/ice interface, are under active investigation. Future experiments will use lower-adiabat pulse shapes like the ramp-to-flat pulse shown in Fig. 90.5 together with targets with recently improved ice layers, to achieve higher areal densities. When the layer quality reaches the design goal of $\sigma_{rms} \leq 1 \mu\text{m}$, low-adiabat pulses like the $\alpha = 3$ pulse will be used to obtain peak areal densities of more than 200 mg/cm^2 using D_2 -ice layers. Table 90.II summarizes the calculated clean 1-D performance and adiabat for the three different pulse shapes. Future cryogenic experiments using DT-ice layers, which are more massive than pure- D_2 layers, should extend the accessible parameter space to peak areal densities of $\sim 300 \text{ mg/cm}^2$.

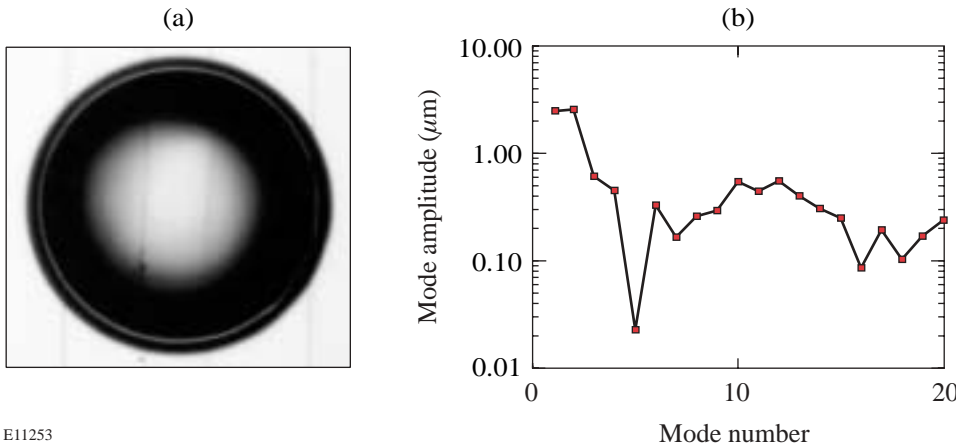


Figure 90.4 Shadowgraphic image (a) of a cryogenic target shown together with the mode-amplitude spectrum (b) of the inner-ice-surface nonuniformities and demonstrating as low as $3\text{-}\mu\text{m}$ rms ice roughness.

E11253

Table 90.II: Calculated clean 1-D performance of D_2 cryogenic target for three pulse shapes with different predicted fuel adiabats. The hot-spot convergence ratio is defined as the ratio of the radius containing 90% of the yield compared to the initial ice interface when propagating burn was deactivated.

Pulse	Adiabat	Energy (kJ)	$\langle \rho R \rangle_{\text{peak}}$ (mg/cm^2)	D_2 yield	Hot-spot CR
1-ns square	27	24	43	1.0×10^{11}	10
Ramp to flat	17	18	63	1.2×10^{11}	11
$\alpha = 3$	3	30	212	8.8×10^{11}	20

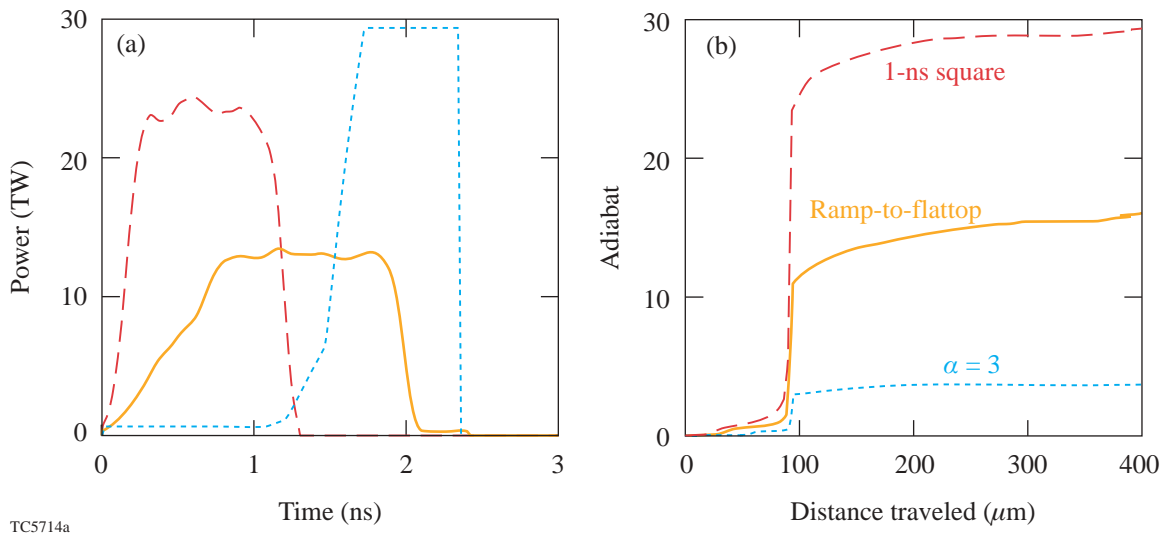


Figure 90.5

Laser power history (a) for three different OMEGA pulse shapes and (b) the corresponding fuel-adiabat trajectories.

Conclusion

The first experiments with the recently commissioned OMEGA Cryogenic Target Handling System have been described. The cryogenic target design is energy scaled from the direct-drive ignition designs for the NIF. The major goal of these experiments is to study the various sources of nonuniformity and their influence on target performance. Similar one-dimensional behavior and stability properties of the OMEGA and NIF cryogenic target designs will facilitate the extrapolation of the cryogenic target studies on OMEGA to NIF targets. In particular, NIF direct-drive ignition targets will be less sensitive to instability growth because the hot spot in the NIF design is bigger than in the OMEGA cryogenic targets. The first cryogenic targets, using 1-ns square pulses, achieved 30% of 1-D yield and more than 60% of the predicted neutron-averaged areal density with an inner-ice-surface nonuniformity of $\sigma_{\text{rms}} = 9 \mu\text{m}$. At the present level of inner-ice-surface nonuniformity, the target performance is strongly affected by the quality of the inner ice layer. Recent improvements in the layering technique make it possible to produce much better ice layers, $\sigma_{\text{rms}} = 3 \mu\text{m}$, with the prospect of achieving the design goal of $1 \mu\text{m}$ in the near future. Targets with improved inner-ice-surface quality will be used with lower-adiabat pulses to substantially increase the fuel areal density. In summary, these very encouraging initial results are a major step on the path leading to high-density compressed cores in direct-drive target implosions on OMEGA and to direct-drive ignition on the National Ignition Facility.

ACKNOWLEDGMENT

The authors are grateful to the staff of the Laboratory for Laser Energetics for their dedicated efforts in developing and providing the high-performance OMEGA laser system, and the tremendous amount of work done in the area of target fabrication to provide as many high-quality cryogenic targets as possible. This work was supported by the U.S. Department of Energy Office of Inertial Confinement Fusion under Cooperative Agreement No. DE-FC03-92SF19460, the University of Rochester, and the New York State Energy Research and Development Authority. The support of DOE does not constitute an endorsement by DOE of the views expressed in this article.

REFERENCES

1. J. A. Paisner, E. M. Campbell, and W. J. Hogan, Lawrence Livermore National Laboratory, Livermore, CA, UCRL-JC-117397 (1994).
2. C. P. Verdon, *Bull. Am. Phys. Soc.* **38**, 2010 (1993).
3. P. W. McKenty, V. N. Goncharov, R. P. J. Town, S. Skupsky, R. Betti, and R. L. McCrory, *Phys. Plasmas* **8**, 2315 (2001).
4. J. Nuckolls *et al.*, *Nature* **239**, 139 (1972).
5. T. R. Boehly, D. L. Brown, R. S. Craxton, R. L. Keck, J. P. Knauer, J. H. Kelly, T. J. Kessler, S. A. Kumpan, S. J. Loucks, S. A. Letzring, F. J. Marshall, R. L. McCrory, S. F. B. Morse, W. Seka, J. M. Soures, and C. P. Verdon, *Opt. Commun.* **133**, 495 (1997).
6. J. D. Lindl, *Inertial Confinement Fusion: The Quest for Ignition and Energy Gain Using Indirect Drive* (Springer-Verlag, New York, 1998), Chap. 6, pp. 61–82.
7. Lord Rayleigh, *Proc. London Math Soc.* **XIV**, 170 (1883).

8. G. Taylor, Proc. R. Soc. London Ser. A **201**, 192 (1950).
9. T. M. Henderson and R. R. Johnson, Appl. Phys. Lett. **31**, 18 (1977).
10. F. J. Marshall, S. A. Letzring, C. P. Verdon, S. Skupsky, R. L. Keck, J. P. Knauer, R. L. Kremens, D. K. Bradley, T. Kessler, J. Delettrez, H. Kim, J. M. Soures, and R. L. McCrory, Phys. Rev. A **40**, 2547 (1989).
11. R. R. Johnson *et al.*, Phys. Rev. A **41**, 1058 (1990).
12. Y. Kitagawa *et al.*, Phys. Rev. Lett. **75**, 3130 (1995).
13. K. A. Tanaka *et al.* Phys. Plasmas **2**, 2495 (1995).
14. K. A. Brueckner and S. Jorna, Rev. Mod. Phys. **46**, 325 (1974).
15. Laboratory for Laser Energetics LLE Review **82**, 49, NTIS document No. DOE/SF/19460-344 (2000). Copies may be obtained from the National Technical Information Service, Springfield, VA 22161.
16. Laboratory for Laser Energetics LLE Review **81**, 6, NTIS document No. DOE/SF/19460-335 (1999). Copies may be obtained from the National Technical Information Service, Springfield, VA 22161.
17. T. J. Kessler, Y. Lin, J. J. Armstrong, and B. Velazquez, in *Laser Coherence Control: Technology and Applications*, edited by H. T. Powell and T. J. Kessler (SPIE, Bellingham, WA, 1993), Vol. 1870, pp. 95–104.
18. T. R. Boehly, V. A. Smalyuk, D. D. Meyerhofer, J. P. Knauer, D. K. Bradley, R. S. Craxton, M. J. Guardalben, S. Skupsky, and T. J. Kessler, J. Appl. Phys. **85**, 3444 (1999).
19. S. Skupsky, R. W. Short, T. Kessler, R. S. Craxton, S. Letzring, and J. M. Soures, J. Appl. Phys. **66**, 3456 (1989).
20. D. D. Meyerhofer, J. A. Delettrez, R. Epstein, V. Yu. Glebov, V. N. Goncharov, R. L. Keck, R. L. McCrory, P. W. McKenty, F. J. Marshall, P. B. Radha, S. P. Regan, S. Roberts, W. Seka, S. Skupsky, V. A. Smalyuk, C. Sorce, C. Stoeckl, J. M. Soures, R. P. J. Town, B. Yaakobi, J. D. Zuegel, J. Frenje, C. K. Li, R. D. Petrasso, D. G. Hicks, F. H. Séguin, K. Fletcher, S. Padalino, M. R. Freeman, N. Izumi, R. Lerche, T. W. Phillips, and T. C. Sangster, Phys. Plasmas **8**, 2251 (2001).
21. S. Skupsky and R. S. Craxton, Phys. Plasmas **6**, 2157 (1999).
22. M. C. Richardson, P. W. McKenty, F. J. Marshall, C. P. Verdon, J. M. Soures, R. L. McCrory, O. Barnouin, R. S. Craxton, J. Delettrez, R. L. Hutchison, P. A. Jaanimagi, R. Keck, T. Kessler, H. Kim, S. A. Letzring, D. M. Roback, W. Seka, S. Skupsky, B. Yaakobi, S. M. Lane, and S. Prussin, in *Laser Interaction and Related Plasma Phenomena*, edited by H. Hora and G. H. Miley (Plenum Publishing, New York, 1986), Vol. 7, pp. 421–448.
23. T. E. Blue *et al.*, J. Appl. Phys. **54**, 615 (1983).
24. H. Azechi *et al.*, Appl. Phys. Lett. **49**, 555 (1986).
25. H. Azechi, M. D. Cable, and R. O. Stapf, Laser Part. Beams **9**, 119 (1991).
26. M. D. Cable and S. P. Hatchett, J. Appl. Phys. **62**, 2233 (1987).
27. Laboratory for Laser Energetics LLE Review **83**, 130, NTIS document No. DOE/SF/19460-357 (2000). Copies may be obtained from the National Technical Information Service, Springfield, VA 22161.
28. F. H. Séguin, C. K. Li, D. G. Hicks, J. A. Frenje, K. M. Green, R. D. Petrasso, J. M. Soures, D. D. Meyerhofer, V. Yu. Glebov, C. Stoeckl, P. B. Radha, S. Roberts, C. Sorce, T. C. Sangster, M. D. Cable, S. Padalino, and K. Fletcher, Phys. Plasmas **9**, 2725 (2002).
29. E. L. Alfonso, I. Anteby, and D. R. Harding, Fusion Technol. **38**, 149 (2000).